PAPER

Check for updates

Sub-nL thin-film differential scanning calorimetry chip for rapid thermal analysis of liquid samples†

Sheng Ni,[a] Hanliang Zhu,[c] Pavel Neuzil[c] and Levent Yobas 🆔 *[ab]

Differential scanning calorimetry (DSC) is a popular thermal analysis technique. The miniaturization of DSC on chip as thin-film DSC (tfDSC) has been pioneered for the analysis of ultrathin polymer films at temperature scan rates and sensitivities far superior to those attainable with DSC instruments. The adoption of tfDSC chips for the analysis of liquid samples is, however, confronted with various issues including sample evaporation due to the lack of sealed enclosures. Although the subsequent integration of enclosures has been demonstrated in various designs, rarely did those designs exceed the scan rates of DSC instruments mainly because of their bulky features and requirement for exterior heating. Here, we present a tfDSC chip featuring sub-nL thin-film enclosures integrated with resistance temperature detectors (RTDs) and heaters. The chip attains an unprecedented sensitivity of 11 V W^{-1} and a rapid time constant of 600 ms owing to its low-addenda design and residual heat conduction (~6 μW K^{-1}). We present results on the phase transition of common liquid crystals which we leverage to calibrate the RTDs and characterize the thermal lag with scan rates up to 900 °C min^{-1}. We then present results on the heat denaturation of lysozyme at various pH values, concentrations, and scan rates. The chip can provide excess heat capacity peaks and enthalpy change steps without much alteration induced by the thermal lag at elevated scan rates up to 100 °C min^{-1}, which is an order of magnitude faster than those of many chip counterparts.

Introduction

Differential scanning calorimetry (DSC) is a well-established dynamic method used in many fields including biotechnology, pharmacology, chemistry, biochemistry, and nanoscience.[1] In DSC, heat flow associated with material transitions is differentially measured for a sample of interest with respect to a reference as a function of temperature and time.[1] The method is routinely used in the study of kinetic processes from transformations of macromolecules to glass transitions and the thermodynamic properties of materials.[2] Traditional instruments, however, are bulky, slow, and lack the required sensitivity for measuring small samples due to

[a] *Department of Electronic and Computer Engineering, The Hong Kong University of Science and Technology, Clear Water Bay, Kowloon, Hong Kong SAR, China. E-mail: eelyobas@ust.hk; Fax: +852 2358 1485; Tel: +852 2358 7068*

[b] *Department of Chemical and Biological Engineering, The Hong Kong University of Science and Technology, Clear Water Bay, Kowloon, Hong Kong SAR, China*

[c] *The Ministry of Education Key Laboratory of Micro/Nano Systems for Aerospace, Department of Microsystem Engineering, School of Mechanical Engineering, Northwestern Polytechnical University, Xi'an, 710072, China*

† Electronic supplementary information (ESI) available: Experimental setup; readout unit; extraction of thermal parameters; experimental results; benchmarking; supplementary figures and table. See DOI: https://doi.org/10.1039/d2lc01094a

their large crucible (addenda). Pioneering studies have introduced the concept of thin-film DSC (tfDSC) for probing glass transitions of ultrathin polymer films[3] and the melting properties of metal nanoclusters.[4]

Demonstrations of tfDSCs for liquids are scarce although thin-film calorimetry chips have been reported for measuring the latent heat of vaporization of a water droplet,[5] the heat capacity of lysozyme,[6] thermal decomposition of organic energetic materials,[7] and altered cell metabolism under a chemical stimulus.[8] In these reports, the designs, however, largely adopt an open architecture that lacks well-defined chambers. Calorimetric measurement of liquids with minimal or no evaporation has also been demonstrated through DSC chips offering well-defined fluidic microchambers.[9–13] These chips share a common feature in that twin calorimetric microchambers are often defined in a polydimethylsiloxane (PDMS) block replica-molded and secured on freestanding polymer diaphragms carrying thin-film heaters and thermometers. In these studies, however, the measurement speed, *i.e.*, the scan rate often remained limited to single digit K min^{-1}, which is comparable to the rate of conventional DSCs, due to several factors. First, the utilization of external heating stages or enclosures for temperature scans (off-chip heating) omitted the advantage of a low thermal mass (fast scan) brought by scaling. Second, the relatively bulky polymeric layer

housing sample and reference microchambers added a large thermal mass to a low-addenda unit featuring twin calorimetric diaphragms. Third, the required sample amount ~1 μL, set by the capacity of microchambers, also introduced a large thermal mass. Apart from the speed, the reported sensitivity levels cannot be further improved by performing measurements under vacuum because of the gas permeable layer housing microchambers incompatible with vacuum operation.

We have previously introduced a thin-film calorimeter chip featuring well-defined sub-nL twin microchannels for differential measurements of liquids and revealed the basic thermal characteristics of the chip based on theoretical and experimental treatments.[14,15] We have also showcased the differential measurement capability of the chip by the evaluation of the photothermal transduction efficiency of plasmonic nanoparticles.[15] Here, we further demonstrate its utility as a tfDSC chip (in DSC mode) for the measurement of liquids under a vacuum environment. Specifically, we present results from the phase and conformational transitions of liquid crystals and protein molecules. Our sub-nL tfDSC chip features thin-film twin calorimetric arms, each with a resistive heater and resistance temperature detector (RTD) and a self-enclosed fluidic microchannel all patterned in a double spiral layout (Fig. 1a). The microchannel on either arm protrudes beneath as a shell structure with a submicron wall thickness and thus contributes a negligible addendum to the arm, which has a nominal thickness of 2.5 μm (Fig. 1b). In either arm, a membrane is suspended over a cavity in silicon by a pair of beams extending from its opposing edges. The beam pairs also connect the respective microchannels to fluidic ports on the substrate. The arms and the microchannels are defined by a layer of low-stress silicon nitride (LSN) whereas the thin-film heaters and RTDs are defined by a layer of titanium at a nominal thickness of 300 nm.
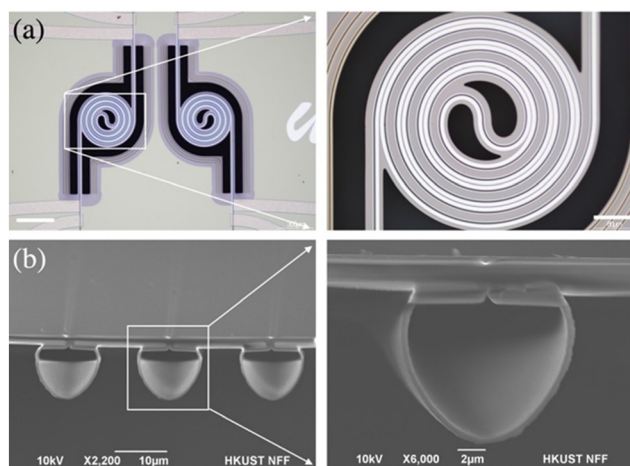
Fig. 1 Sub-nL tfDSC chip. (a) Optical micrographs (planar view) of the twin calorimetric arms (scale: 300 μm) and magnified membrane region (scale: 80 μm). (b) Scanning electron microscopy images (cutaway view) of the membrane revealing the self-enclosed spiraling fluidic microchannel: three spiral turns (scale: 10 μm) and a magnified single turn (scale: 2 μm).

tfDSC principle

Temperature deviations between the sample and reference arms undergoing heating or cooling at a linear constant scan rate signify thermodynamic processes occurring in the sample at characteristic temperatures. A power ramp P simultaneously applied to the heaters raises the temperature of both arms at nearly identical rates.

We can write the heat balance equation for the sample arm as

$$(C_s + C_s^{ex} + C_r)\frac{dT_s}{dt} + (G_s + G_r)(T_s - T_{env}) = P \quad (1)$$

and for the reference arm as

$$C_r\frac{dT_r}{dt} + G_r(T_r - T_{env}) = P \quad (2)$$

where C_s and G_s represent the heat capacity and heat conduction of the sample (e.g., liquid crystals) or solute (protein molecules) loaded into the sample arm, C_r and G_r are the heat capacity and heat conduction of either calorimetric arm, including the background solvent if present, C_s^{ex} is the excess heat capacity of the sample arising from thermodynamic processes, and T_s, T_r and T_{env} represent the temperatures of the sample and reference arms and the ambient temperature, respectively. The heat capacities are assumed constant, independent of time and temperature.

Under the assumption of identical temperature scan rates for the sample and reference arms, eqn (1) and (2) can be combined to give the sample excess heat flow rate as

$$C_s^{ex}\frac{dT_s}{dt} = C_s\frac{dT_s}{dt} - G_s(T_s - T_{env}) - G_r\Delta T \quad (3)$$

where the last term on the right-hand side contains the measured quantities, G_r and $\Delta T = T_s - T_r$, whereas the first and second terms appear in the thermograms as the bias and linear contributions. Both terms can be subtracted through curve fitting. For common mode rejection, the differential temperature ΔT is measured using a half Wheatstone bridge circuit featuring the resistance temperature detectors (RTDs) of the sample and reference arms and the output processed by a differential amplifier. During a scan, the ΔT value is continuously measured as a function of T_r based on the amplified output voltage ΔV:

$$\Delta T = (1/\alpha + T_r)\frac{4\Delta V}{BV_B} \quad (4)$$

with α being the temperature coefficient of resistance (TCR) of the RTDs (as well as the thin-film heaters), B the gain of the differential amplifier, and V_B the bridge RMS bias voltage.

The excess heat capacity of sample C_s^{ex} can be calculated as a function of the temperature of the sample from eqn (3) by normalizing both sides with the scan rate. Integrating the excess heat capacity associated with a thermodynamic process over temperature with the limits of integration from

the onset temperature of the process T_i to its completion temperature T_f yields the resulting specific enthalpy change

$$\Delta H = \int_{T_i}^{T_f} C_s^{ex}(T)\mathrm{d}T \qquad (5)$$

Methods and experimental

Microfabrication

We designed the sub-nL tfDSC chip using the Nanolithography Toolbox[16,17] and fabricated it as previously reported[15] on 100 mm diameter silicon wafers through a cleanroom process based on the buried channel technology.[18] We used wafers having a 1-μm-thick layer of LSN received through low pressure chemical vapor deposition (LPCVD). We etched fluidic microchannels into silicon in SF_6 plasma through 800 nm-wide slits patterned in the LSN layer in a double spiral layout in a photolithography step involving UV exposure in a stepper (PAS 5000/55, ASML, Veldhoven, The Netherlands). Subsequently, we sealed off the slits with another layer of LSN deposited 1.5 μm thick *via* LPCVD to enclose the channels while forming the nitride channel walls. We sputtered and patterned a thin-film Al 1 μm thick and then a thin-film Ti 300 nm thick with the latter serving as thin-film RTDs and heaters on twin arms while the former being removed from the twin arms serving as a support layer lowering the electrical resistance of Ti lead outs. After a lithography step patterning fluidic ports and release vias, we performed reactive ion etching and XeF_2 release of the twin arms on individual chips singulated from wafers. We plasma-ashed the photoresist layer and then mounted each chip on a printed circuit board (PCB) before performing wire bonding to contact pads. Fig. S1a† shows a photograph of the sub-nL tfDSC chip mounted on a PCB and an optical micrograph of the overall chip.

Materials

We obtained 4-cyano-4′-pentylbiphenyl (5CB) and 4-heptyl-4′-cyanobiphenyl (7CB) liquid crystals from QY Liquid Crystal Co., Ltd. (Qingdao, China), freeze-dried egg-white lysozyme powder for molecular biology from neoFroxx GmbH (Einhausen, Germany), glycine from Sigma Aldrich (Darmstadt, Germany), PDMS from Dow Corning (Midland, MI), and epoxy from Henkel (Düsseldorf, Germany).

Sample preparation

We used liquid crystals as procured without further processing. We dissolved 7.5 g glycine powder in 800 mL deionized water before adding 40 mL 0.1 M HCl to obtain a 100 mM Gly-HCl buffer solution. We adjusted the pH to desired levels by adding HCl or NaOH based on readings from a pH meter (Smart Sensor PH828+, Wanchuang Electronic, Dongguan, China). We then brought up the volume to 1 L by adding deionized water. We dissolved lysozyme powder to desired concentrations in the prepared Gly-HCl buffer. Before use, we degassed the solutions in a vacuum desiccator for about two hours.

Sample infusion

We introduced lysozyme and buffer solutions into the respective arms with the aid of a microfluidic manifold replicated into PDMS through soft lithography. We secured the manifold on the inlet ports using an acrylic fixture and then gently infused the solutions into the arms from syringes until the solutions emerged at the outlet ports. We applied and cured epoxy on the outlet ports before removing the manifold and then similarly applied and cured epoxy on the inlet ports. We also followed this procedure to infuse the liquid crystals into the sample arms which we measured against blank reference arms.

Experimental setup

We placed the prepared sub-nL tfDSC chip inside an enclosure for further thermal isolation before placing the enclosure as well as the readout circuit interfacing the chip inside a custom-made vacuum chamber (Fig. S1b†) linked to a turbomolecular pump (Turbo-V70, Varian, Lexington, MA). We then rested the vacuum chamber inside a styrofoam box filled with ice packs (NOR1038, Nordic Cold Chain Solutions, Reno, NV) to set the onset temperature of scans to about 10 °C. The readout circuit contained a half Wheatstone bridge featuring the sensing and reference RTDs and a differential amplifier (Fig. S1c†). The experimental setup along with the readout circuit (Fig. S2†) and the bridge balancing procedure is further described in the ESI.†

Measurements

We first measured the resistance values of the thin-film RTDs and heaters against the temperatures of the respective arms, which we set with 0.1 °C precision by means of heat supplied from a probe station. We then normalized each measurement with the respective values measured at room temperature and we evaluated the TCR based on the normalized values. Subsequently, we extracted the thermal parameters of the twin arms based on the long pulse method as described in our previous work[15] and presented in the ESI† (Fig. S3). We used a source measure unit (Keithley 2612B, Tektronix, Beaverton, OR) driven by a custom LabVIEW program to supply voltages to the thin-film heaters on the arms while monitoring the respective current levels to estimate the absolute temperature of the arms. We used a lock-in amplifier (HF2IS, Zurich Instruments, Zurich, Switzerland) to bias the Wheatstone bridge with a reference sinewave voltage at about 1 kHz and a 100 mV peak. We amplified the bridge output voltage with a gain of 991 from a differential amplifier (AD8221BRZ, Analog Devices, Cambridge, MA). We applied the lock-in demodulation with a time constant of 71.2 ms and a filter slope of 24 dB per octave. We performed a linear temperature scan at specified rates by applying a power ramp

to both heaters and measured the differential temperature of the twin arms as a function of temperature and time. We recorded the demodulated signal into a computer and then processed the data offline through a custom Python program to plot thermograms. We removed the baseline from the thermograms using OriginPro 2021 (OriginLab, Northampton, MA).

Results and discussion

Basic characteristics

We determined the TCR of the RTDs, α, and the heat conduction of the reference arm, G_r, before differential measurements. The former is required for mapping the bridge output voltage ΔV to the differential temperature ΔT between the twin arms [eqn (4)] and the latter for evaluating the sample excess heat flow and the corresponding excess heat capacity, C_s^{ex} [eqn (3)]. We measured $\alpha \sim 0.372\%$ K^{-1} based on the transfer curve of the RTDs (Fig. 2a). This TCR value compares well to those reported for Ti thin films.[19] We extracted the thermal parameter values of the twin arms and obtained a thermal time constant value of $\tau \sim 600$ ms and a heat conduction value of $G_r \sim 5.07$ μW K^{-1} for a blank arm at room temperature under vacuum. We also measured the same arm after being filled with a solvent (100 mM Gly-HCl buffer, pH 2.5) and observed only a slight increase. However,

we noticed a non-negligible increase in the G_r value in a linear trend with temperature within the scan range and we took this temperature dependence into account for the accuracy of calorimetric measurements (Fig. 2b).

Prior to the measurements, we performed noise analysis to optimize the lock-in amplification. We recorded the heat flow for a duration of over three hours with the twin arms filled with 100 mM Gly-HCl buffer (pH, 2.5) and kept at room temperature under vacuum. Fig. 2c and d show the recordings (baseline removed) and the corresponding Allan deviation (ADEV) curves (before the baseline removal) obtained using various lock-in amplifier settings (legend). At a bandwidth of 300 Hz, the lock-in integration time (<1 ms) is insufficient to filter out the white noise which shows up as a negative slope in the corresponding ADEV curve. Lowering the filter bandwidth leads to a major reduction in noise but extensive lowering (<1 Hz) deteriorates the thermal resolution because the lock-in time constant (>1 s) exceeds the thermal time constant of our chip ($\tau \sim 600$ ms). Thus, in all our measurements, we set the lock-in filter bandwidth to 1 Hz, thereby limiting the nominal RMS noise level to 8 nW and the bias instability to 1.46 nW s^{-1}.

Calibration on liquid crystals

We calibrated our tfDSC chip by measuring the phase-transition heats of nematic liquid crystals: alkylcyanobiphenyl (nCB, where n signifies the number of carbon atoms in the alkyl chain). We specifically used 4-cyano-4′-pentylbiphenyl (5CB) and 4-heptyl-4′-cyanobiphenyl (7CB). Both 5CB and 7CB exist in the nematic phase at room temperature and undergo a nematic-to-isotropic (N–I) phase transition within the interval of 35 °C to 45 °C. The N–I phase transition shows up as an endothermic peak in the thermograms of 5CB and 7CB measured using an adiabatic scanning calorimeter at 35.29 °C and 42.73 °C, respectively, with the corresponding latent heats 1.56 and 2.03 J g^{-1}.[20] The calibration data based on the phase transition temperatures of 5CB and 7CB concur well with the calibration data obtained in our previous study based on the melting temperatures of nucleic acids of two distinct sequences.[14] Collectively, the calibration data suggest an apparent value of $\alpha \sim 0.306\%$ K^{-1} that can accurately map the measured RTD values to the respective temperatures inside the calorimetric arms.

Fig. 3a shows the DSC thermograms of 5CB and 7CB obtained from the amplified bridge output (baseline subtracted). We obtained the traces by performing scans under vacuum at a rate of 10 °C min^{-1} on identical chips with sample arms that contained either 5CB or 7CB and reference arms left blank. Both of the traces show well-defined endothermic peaks for the N–I phase transitions of 5CB and 7CB. Using eqn (3) and (4), we converted these traces into heat flow plots and compared them to those obtained from a commercial DSC instrument; the plots are shown normalized by the sample mass in Fig. 3b. We estimated the sample mass based on the specific mass of 5CB and 7CB (ρ = 1.01 g cm^{-3} for both) and the arm capacity
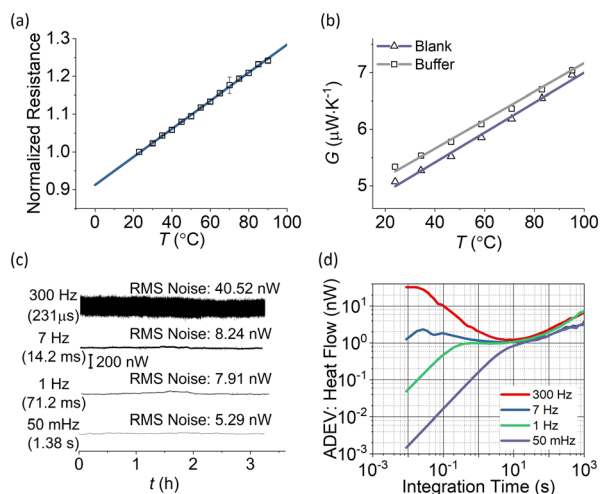
Fig. 2 Basic characteristics. (a) Transfer plot of the RTDs based on the measured resistance values at elevated temperatures normalized by the value measured at room temperature. The symbols represent the means of the measurements from four pairs of RTDs with error bars mostly indiscernible. The linear fitting slope returns a TCR value of 0.372% K^{-1}. (b) Temperature dependence of the heat conduction through one of the twin arms measured first as blank and then filled with a Gly-HCl buffer (100 mM; pH, 2.5). (c) Representative heat flow traces (baseline removed) obtained with the lock-in filter bandwidth set at 0.05, 1, 7, and 300 Hz and the corresponding time constant values listed in the parentheses. (d) Plot of the corresponding ADEV curves before the baseline removal. In (c) and (d) the measurements made at room temperature under vacuum with the arms filled with a Gly-HCl buffer (100 mM; pH, 2.5). In (c) scale bar: 200 nW.
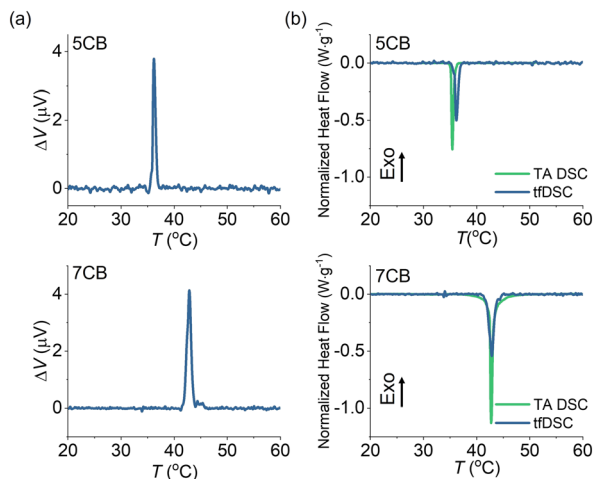
Fig. 3 DSC thermograms of liquid crystals 5CB and 7CB obtained from sub-nL tfDSC chips (baseline subtracted) and from a commercial instrument (TA Instruments, DSC Q1000). Endothermic heat flow peaks are associated with the N–I phase transition of 5CB and 7CB: (a) the amplified bridge output traces over the scanned temperature range and (b) the corresponding normalized heat flow plots in comparison with those obtained from the commercial unit for 5CB (upper row) and 7CB (lower row). Scan rate: 10 °C min⁻¹.

($\sim$420 pL) defined by the channel length on the membrane and the cross-sectional channel dimensions measured on the images (Fig. 1b). The plots indicate the N–I phase transition temperatures for 5CB and 7CB as 35.43 °C and 42.73 °C from a commercial unit and 36.19 °C and 42.86 °C from tfDSC chips, respectively. These values concur with previous reports.[20]

In Fig. 4, the plots of the corresponding excess heat capacity C_s^{ex} [eqn (3) normalized by the scan rate] and enthalpy change ΔH [eqn (5)] against the temperature are shown. In Fig. 4b, the resultant enthalpy change values are
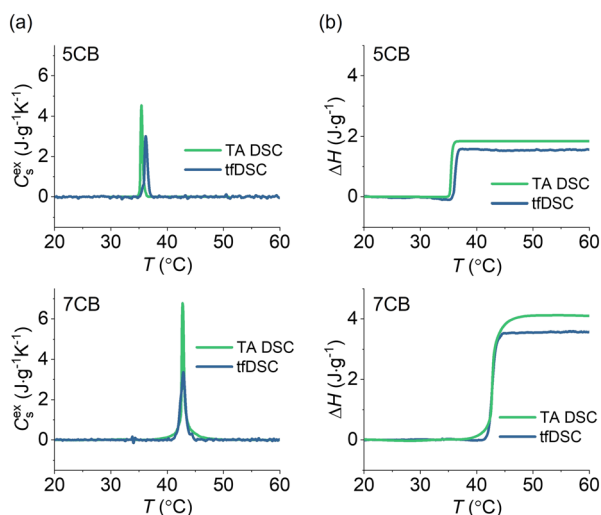
Fig. 4 (a) Excess heat capacity and (b) enthalpy change as a function of the temperature obtained during the N–I phase transition of 5CB (upper row) and 7CB (lower row) from tfDSC chips (baseline subtracted) and the commercial DSC system. Scan rate: 10 °C min⁻¹.

comparable despite the sharp and tall peaks obtained by the commercial DSC and relatively broad peaks obtained by the tfDSC chips. We attribute the broad profile of the tfDSC peaks to the temperature gradient within the calorimetric arms and the consequent spatial evolution of the phase transition; the phase transition starts near the membrane center and then gradually spreads as the temperature is increased. Thus, the heat required for the N–I phase transition gets dissipated gradually, leading to a broadened peak. The corresponding enthalpy change for either liquid crystal falls below the value measured by the commercial unit and yet agrees well with the reported values. In particular, an enthalpy change noted for 5CB in the amount of 1.55 J g⁻¹ is in good agreement with the values reported in the range of 1.56–2.10 J g⁻¹.[20–22] For 7CB, however, the amount of 3.54 J g⁻¹ is slightly larger than those typically reported in the range of 2.03–3.22 J g⁻¹.[20,22]

Thermal lag

Like all other low-addenda calorimetric sensors, a clear advantage of the sub-nL tfDSC chip is that it can conduct measurements at high scan rates. Although a high scan rate induces a strong signal, it also brings thermal gradients (thermal lag) and leads to smeared phase transition peaks (excess heat capacity) and steps (enthalpy change).[2] The influence of increased scan rates on the tfDSC curves is revealed in Fig. 5. The N–I phase transition peaks and steps obtained for 5CB and 7CB at a scan speed of up to 100 °C min⁻¹ show a moderate smearing in reference to those obtained at 20 °C min⁻¹ (Fig. 5a). A strong smearing, however, is noted for the curves obtained at 200 °C min⁻¹ and beyond (Fig. 5b). The latter set of curves becomes increasingly distorted with scan speed; the peaks spread and shift to elevated temperatures albeit the respective peak areas, i.e., the total enthalpy change, are nearly preserved. The steps assume a sigmoidal shape without major alterations in the total enthalpy change. Because of the low thermal inertia of the twin arms, the tfDSC chip can accommodate scan speeds up to 100 °C min⁻¹ before the smearing becomes intolerable. For the results obtained at rates in excess of 100 °C min⁻¹, de-smearing procedures[23] can be applied to minimize the thermal lag influence. The fast scan capability of the tfDSC chip enhances the sensitivity while shortening the analysis time compared to commercial instruments.

Using Kissinger plots (Fig. 6), we have explored the scan rate dependence of the endothermic peak positions of the N–I phase transitions. These plots relate the transition peak temperature and scan rate through the Arrhenius equation:[24]

$$\ln\left(\frac{\beta}{T_p^2}\right) = \beta_0 + \frac{E_a}{RT_p} \quad (6)$$

where β is the scan rate (K min⁻¹), β_0 is a constant, E_a is the apparent activation energy (J mol⁻¹), R is the universal gas
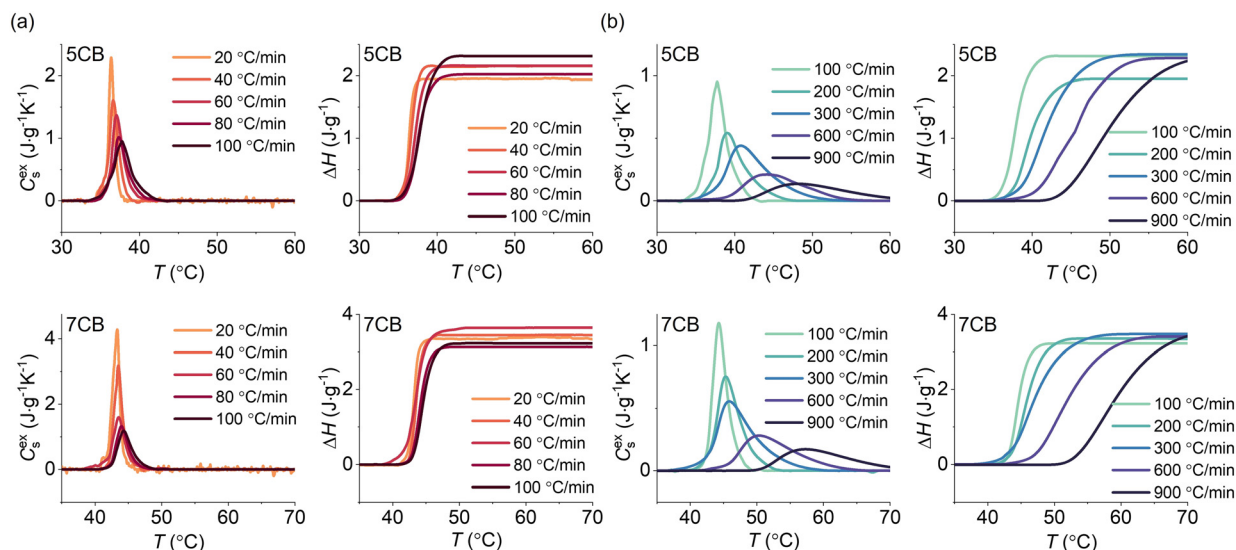
Fig. 5 The influence of tfDSC scan rate on the excess heat capacity peaks and enthalpy change steps. (a) Moderate and (b) excessive smearing observed for the N–I phase transition peaks and steps for 5CB (upper rows) and 7CB (lower rows) based on the scan rate values (legends).

constant (8.31 J mol^{-1} K^{-1}) and T_p is the phase transition peak temperature (K).

The plots can be divided into three regions. These are the regions of rapid and slow scans and an intermediate transition region. In the region of slow scan, the peak temperature shows weak dependence on the scan speed and, instead, is dictated by the phase transition kinetics of the liquid crystals. In the region of rapid scan, however, it shows strong dependence on the scan speed and is dominated by the tfDSC thermal lag. The phase transition kinetics of 5CB and 7CB can be derived from the slow scan region with the corresponding slope providing the apparent activation energy E_a. This energy represents a constant barrier against the N–I phase transition. The phase transitions of 5CB and 7CB show a negative slope due to the endothermic nature of the process, both with similar energy requirements, 1.58 and 1.67 kJ mol^{-1}, respectively. The value for 5CB is in reasonable agreement with 1.68 kJ mol^{-1}, the quantity reported[25] based

on scan rates in the range of 5–20 °C min^{-1}, while the corresponding energy requirement value for 7CB cannot be found in the literature. In the region where the thermal lag dominates (rapid heating), both 5CB and 7CB show a diminished slope (E_a) suggesting that their phase transition rate is not limited by a temperature-dependent reaction rate constant. Rather, it is limited by the heat conduction through the calorimetric arm.

Protein denaturation

We next showed the utility of our tfDSC chip on the study of thermally induced denaturation of protein molecules, *i.e.*, the conformational transitions of protein unfolding. We used lysozyme, specifically hen egg-white lysozyme (MW 14307), a commonly studied model protein with an abundance of thermodynamics data in the literature.[26]

We obtained thermograms from identical chips placed under vacuum with their sample arms loaded with lysozyme dissolved in 100 mM Gly-HCl buffer (pH, 2.5) and their reference arms with the same solvent but without the dissolved lysozyme. For lysozyme concentrations of 30, 50, 100, and 200 mg mL^{-1}, we measured the heat flow while scanning the twin arms at a constant rate of 60 °C min^{-1} in the range of 10–90 °C (Fig. 7a). We observed the endothermic peaks growing linearly with the lysozyme concentration (Fig. 7b). We then derived the excess heat capacity [eqn (3)] and enthalpy change [eqn (5)] associated with the denaturation process against temperature (Fig. 7c). We noted a concentration-dependent increase in the denaturation temperature from 67.7 °C to 73.1 °C which we attributed to increased excluded volume interactions of lysozyme molecules and the respective increase in the energy requirement for denaturing transitions.[27] We also noted a rise in the enthalpy change from 416.6 to 485.7 kJ mol^{-1} with the increase of lysozyme concentration from 30 to 50 mg mL^{-1} and
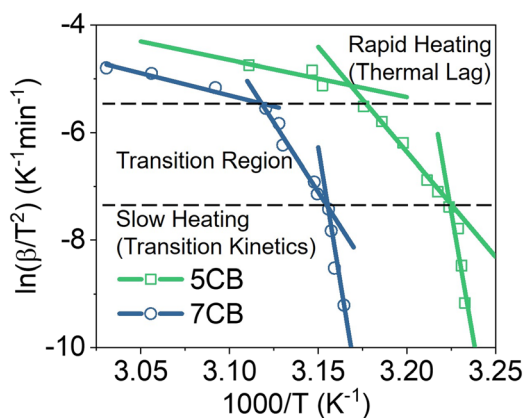
Fig. 6 Kissinger plots relating the N–I phase transition peak temperatures of 5CB and 7CB (legends) to the tfDSC scan speed.
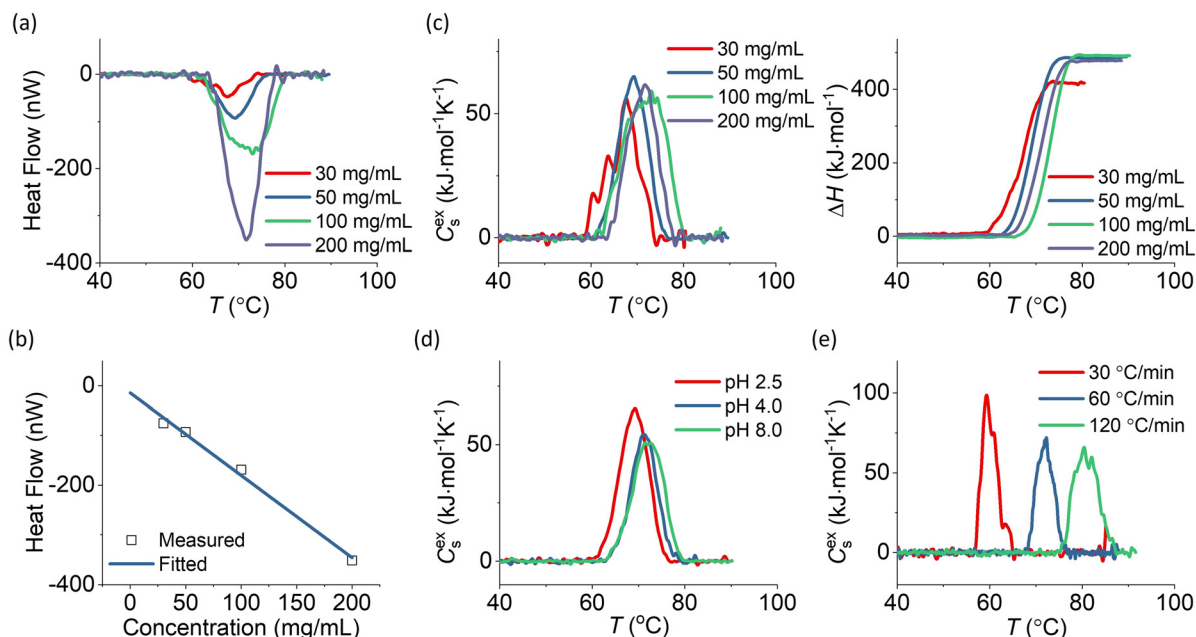
Fig. 7 DSC thermograms of lysozyme molecules obtained from tfDSC chips as they undergo thermal denaturation. (a) Heat flow plots (baseline subtracted) and (b) the peak heat flow against the lysozyme concentration obtained for lysozyme solutions at pH 2.5 and the concentrations as specified (legend). (c) The corresponding excess heat capacity and enthalpy change against temperature. (d) and (e) Excess heat capacity against temperature for lysozymes (d) at 100 mg mL^{-1} and various pH values (legend) and (e) at 50 mg mL^{-1} and pH 2.5, with each peak corresponding to a distinct scan rate (legend). Scan rate: 60 °C min^{-1} unless otherwise stated.

noted the value that remained thereafter (fluctuation, ±10 kJ mol^{-1}) for concentrations above 50 mg mL^{-1}. These results compare favorably with those previously reported (listed below). Previous reports also revealed the pH-dependence of the denaturation temperature; the denaturation temperature increases with increased pH from 2.0 to 4.0, owing to the α helix conformation becoming more stable.[28] Our results concur with these findings as we observed a similar trend when we increased the pH from 2.5 to 4.0 while keeping the lysozyme concentration at 100 mg mL^{-1} (Fig. 7d). Further elevation to pH 8.0, however, returned no net effect possibly due to the compromised thermal stability of lysozyme molecules caused by their pH-induced aggregation.[28]

Our results are in line with those previously reported based on commercial DSC instruments. Wu *et al.*[29] reported a denaturation temperature of about 75 °C and an enthalpy change of 427.8 kJ mol^{-1} for lysozymes at pH ~ 3 and concentrations above 15 mg mL^{-1} (scan rate, 1.0 °C min^{-1}). Schwarz[26] reported 64.0 °C and 440.7 kJ mol^{-1} for lysozymes at pH ~ 3 (scan rate, 0.3 °C min^{-1}). The values also differ with different scan rates. We observed that the endothermic peak position shifted to a reduced temperature with a reduced scan rate or *vice versa* (Fig. 7e). The scan rate dependence of the peak position is more dramatic in the case of lysozyme denaturation than liquid crystal phase transition (Fig. 5a). This is mainly because of the slow kinetics of the former[30] in relation to the fast kinetics of the latter.[31]

The tfDSC chip can also achieve comparable scan rates on cooling. We obtained thermograms of 5CB and 7CB from single heating–cooling cycles with heating and cooling at

identical scan rates. In the thermograms, the I–N phase transition shows up as an exothermic peak during cooling (Fig. S4†). For thermal analysis, it is critical to compare the heating and cooling cycles and check for the symmetry of thermal lag in the two cycles. The symmetry occurs when the scan rate equally influences the transition peak temperatures in heating and cooling.[32] Under the symmetry, the thermal lag correction applied for the heating cycle can also be applied for the cooling cycle without any additional calibration. For symmetry verification, liquid crystals with transition peak temperatures showing no or very small superheating and supercooling can be used.[33] Here, tfDSC behaves in a more or less symmetrical manner based on the phase transition peaks of 5CB and 7CB in heating and cooling (Fig. S5†).

The cooling rate under vacuum operation is limited by the system thermal time constant and the temperature difference between the calorimetric arms and the substrate. Although the cooling rate can be enhanced by active cooling under liquid nitrogen or gas coolant,[34] excessive smearing is encountered for the peaks obtained at −200 °C min^{-1} and beyond (Fig. S4†). This issue could be addressed by further reducing the lateral dimensions of the calorimetric membranes. Fast scanning on cooling is important for the study of the phase formation of metastable materials in processes such as crystallization, amorphization and gelation at quenching.[35]

Lastly, the tfDSC chip can be readily integrated with microfluidics as it shares common fabrication steps with other microfluidic devices.[36] For instance, the tfDSC chip can

be integrated with a micromixer to measure mixing enthalpies based on the differential heat flux into to the sample and reference arms in isothermal mode (differential isothermal calorimetry).[37]

Conclusions

We have demonstrated a sub-nL tfDSC chip for the thermal analyses of liquid samples. This is the first tfDSC chip that features thin-film enclosures, thus exhibiting very low-addenda heat capacity and similarly low residual heat conduction. The chip has a very rapid temperature response which we take full advantage of by performing temperature scans through on-chip heating. Compatible with vacuum operation, the chip outperforms many of its counterparts in terms of sensitivity, time constant, scan rate, noise and sample amount requirement as seen in the benchmarking results in Fig. S6 and Table S1.† These merits could render this powerful thermoanalysis technique applicable to areas where it is currently out of reach due to its limited scan rate and sensitivity.

Author contributions

Sheng Ni and Levent Yobas: conceptualization. Sheng Ni, Hanliang Zhu, Pavel Neuzil, and Levent Yobas: methodology. Sheng Ni: experiment, data curation, algorithm, writing – original draft preparation, and device fabrication. Levent Yobas: supervision. All authors: writing – review and editing.

Conflicts of interest

There are no conflicts to declare.

Acknowledgements

References

1 P. Gill, T. T. Moghadam and B. Ranjbar, *J. Biomol. Tech.*, 2010, **21**, 167–193.

2 G. W. H. Höhne, W. F. Hemminger and H. J. Flammersheim, *Differential Scanning Calorimetry*, Springer-Verlag, Berlin, second edn, 2003.

3 M. Y. Efremov, E. A. Olson, M. Zhang, Z. S. Zhang and L. H. Allen, *Macromolecules*, 2004, **37**, 4607–4616.

4 M. Y. Efremov, F. Schiettekatte, M. Zhang, E. A. Olson, A. T. Kwan, R. S. Berry and L. H. Allen, *Phys. Rev. Lett.*, 2000, **85**, 3560–3563.

5 E. B. Chancellor, J. P. Wikswo, F. Baudenbacher, M. Radparvar and D. Osterman, *Appl. Phys. Lett.*, 2004, **85**, 2408–2410.

6 J. L. Garden, E. Château and J. Chaussy, *Appl. Phys. Lett.*, 2004, **84**, 3597–3599.

7 N. W. Piekiel, R. E. Cavicchi and M. R. Zachariah, *Thermochim. Acta*, 2011, **521**, 125–129.

8 E. A. Johannessen, J. M. Weaver, L. Bourova, P. Svoboda, P. H. Cobbold and J. M. Cooper, *Anal. Chem.*, 2002, **74**, 2190–2197.

9 L. Wang, B. Wang and Q. Lin, *Sens. Actuators, B*, 2008, **134**, 953–958.

10 B. Wang and Q. Lin, *J. Microelectromech. Syst.*, 2012, **21**, 1165–1171.

11 B. Wang and Q. Lin, *Sens. Actuators, B*, 2013, **180**, 60–65.

12 S. Wang, S. Yu, M. S. Siedler, P. M. Ihnat, D. I. Filoti, M. Lu and L. Zuo, *Rev. Sci. Instrum.*, 2016, **87**, 105005.

13 S. Wang, S. Yu, M. Siedler, P. M. Ihnat, D. I. Filoti, M. Lu and L. Zuo, *Sens. Actuators, B*, 2018, **256**, 946–952.

14 S. Ni, H. Zhu, P. Neuzil and L. Yobas, *J. Microelectromech. Syst.*, 2020, **29**, 1103–1105.

15 S. Ni, Y. Bu, H. Zhu, P. Neuzil and L. Yobas, *J. Microelectromech. Syst.*, 2021, **30**, 759–769.

16 H. Zhang, J. Pekárek, J. Feng, X. Liu, H. Li, H. Zhu, V. Svatoš, I. Gablech, P. Podešva and S. Ni, *J. Vac. Sci. Technol., B*, 2020, **38**, 063002.

17 K. C. Balram, D. A. Westly, M. Davanco, K. E. Grutter, Q. Li, T. Michels, C. H. Ray, L. Yu, R. J. Kasica and C. B. Wallin, *J. Res. Natl. Inst. Stand. Technol.*, 2016, **121**, 464.

18 M. J. de Boer, R. W. Tjerkstra, J. W. Berenschot, H. V. Jansen, C. J. Burger, J. G. E. Gardeniers, M. Elwenspoek and A. van den Berg, *J. Microelectromech. Syst.*, 2000, **9**, 94–103.

19 B. Singh and N. A. Surplice, *Thin Solid Films*, 1972, **10**, 243–253.

20 J. Thoen, G. Cordoyiannis and C. Glorieux, *Liq. Cryst.*, 2009, **36**, 669–684.

21 B. Van Roie, J. Leys, K. Denolf, C. Glorieux, G. Pitsi and J. Thoen, *Phys. Rev. E: Stat., Nonlinear, Soft Matter Phys.*, 2005, **72**, 041702.

22 G. A. Oweimreen and M. A. Morsy, *Thermochim. Acta*, 2000, **346**, 37–47.

23 A. Sommer, W. Hohenauer and T. Barz, *J. Therm. Anal. Calorim.*, 2022, **147**, 11477–11492.

24 H. E. Kissinger, *Anal. Chem.*, 1957, **29**, 1702–1706.

25 D. Sharma, *J. Therm. Anal. Calorim.*, 2010, **102**, 627–632.

26 F. P. Schwarz, *Thermochim. Acta*, 1989, **147**, 71–91.

27 A. P. Minton, *Biophys. J.*, 2005, **88**, 971–985.

28 S. Venkataramani, J. Truntzer and D. R. Coleman, *J. Pharm. BioAllied Sci.*, 2013, **5**, 148–153.

29 S. Wu, Y. Ding and G. Zhang, *J. Phys. Chem. B*, 2015, **119**, 15789–15795.

30 D. V. Laurents and R. L. Baldwin, *Biochemistry*, 1997, **36**, 1496–1504.

31 Y. V. Sperkach, V. S. Sperkach, O. Aliokhin, A. L. Strybulevych and M. Masuko, *Mol. Cryst. Liq. Cryst.*, 2001, **366**, 183–202.

32 M. Chen, M. Du, J. Jiang, D. Li, W. Jiang, E. Zhuravlev, D. Zhou, C. Schick and G. Xue, *Thermochim. Acta*, 2011, **526**, 58–64.

33 S. Wouters, F. Demir, L. Beenaerts and G. Van Assche, *Thermochim. Acta*, 2012, **530**, 64–72.

34 S. A. Adamovsky, A. A. Minakov and C. Schick, *Thermochim. Acta*, 2003, **403**, 55–63.

35 C. Schick and R. Androsch, in *Recent Advances, Techniques and Applications*, ed. S. Vyazovkin, N. Koga and C. Schick, Elsevier, Netherlands, 2018, ch. 2, vol. 6, pp. 47–102.

36 J. Groenesteijn, M. J. de Boer, J. C. Lötters and R. J. Wiegerink, *Microfluid. Nanofluid.*, 2017, **21**, 127.

37 P. Jablonski, A. Muller-Blecking and W. Borchard, *J. Therm. Anal. Calorim.*, 2003, **74**, 779–787.

This journal is © The Royal Society of Chemistry 2023